Hard TiAlTaN coating by HIPIMS deposition for cutting tools: experiments, simulations and cutting tests

Emile HAYE^{1,2}, Loris CHAVEE¹, Judith SABATA MAS², Essam SERAG¹, Szilard KOLOZSVARI³, Noé WATIEZ^{1,4}, Aurélien BESNARD^{4,5}, Yoann PINOT⁴, Pavel MOSKOVKIN^{1,2}, Jérôme MULLER^{1,2}, Stéphane LUCAS^{1,2}

Abstract

The quaternary Ti_xAl_yTa_zN system has demonstrated superior thin film properties compared to conventional Ti_xAl_yN coatings. Beyond the influence of Ta content, the deposition method plays a crucial role in determining the structural and mechanical characteristics of the films. In this work, highpower impulse magnetron sputtering (HiPIMS) was used to deposit dense, tough, and hard Ti_xAl_yTa₂N coatings with different compositions from composite targets. These coatings were compared with TiAIN films. The impact of Ta incorporation was investigated both experimentally and through numerical simulations. Thin film growth and composition were modeled using VirtualCoater™, which provided valuable insights into the role of Ta in enhancing film densification and clarified the link between target and film compositions. Subsequent experimental characterization of mechanical, structural, and thermal properties revealed the significant advantages conferred by Ta addition. The improvements are attributed to: (1) enhanced hardness due to densification induced by energetic Ta ion bombardment, (2) stabilization of the cubic phase at elevated temperatures, and (3) improved thermal resistance through the formation of a homogeneous (Ti_xAl_yTa_z) oxide layer, in contrast to the Al₂O₃/TiO₂ bilayer typically observed in TiAlN coatings, as confirmed by XPS depth profiling. Finally, dry cutting tests confirmed a marked increase in tool life and improved surface finish of the machined components.

¹ Laboratoire d'Analyse par Réaction Nucléaires (LARN), Namur Institute of Structured Matter (NISM), University of Namur, 61 Rue de Bruxelles, 5000 Namur, Belgium

² Innovative Coating Solutions (ICS), Rue Jean Sonet 10, 5032 Gembloux, Belgium

³ Plansee Composite Materials GmbH, 86983, Lechbruck am See, Siebenbürgerstr. 23, Germany

⁴ Arts et Metiers Institute of Technology, LaBoMaP, 1" rue porte de Paris, 71250 Cluny, France

⁵ Université Marie et Louis Pasteur, SUPMICROTECH, CNRS, institut FEMTO-ST, F-2500 Besançon, France.

Introduction

Hard coatings based on transition metal nitrides are widely used to enhance the performance of cutting tools by improving their wear resistance, thermal stability, and oxidation behavior. Over the past fifty years, ICMCTF has been an important venue for presenting and explaining the performance of these new coatings. It has been the central place where thin film science meets industrial innovation. Among those coatings, TiAlN has emerged in early 1990s [1], as a reference material due to its high hardness, thermal stability, and favorable tribological properties, along with AlCrN-based coating. However, under high-temperature machining conditions, TiAIN undergoes structural changes through spinodal decomposition into cubic TiN and cubic AlN phases (promoting improved hardness), followed by wurtzite formation, and oxidation; the last process contributes to coating failure [2,3]. These mechanisms start around 600°C to be fully completed at 800°C. Mechanistic studies by Greczynski et al. and Chavee et al. [4,5] have shown that oxidation and phase decomposition occur through distinct mechanisms and are both strongly influenced by temperature and Ti over Al ratio. The addition of tantalum (Ta) into TiAIN system, resulting in TiAITaN coatings, has been shown to significantly improve high-temperature performance [6-8]. Ta incorporation enhances the thermal stability of the cubic phase, delays spinodal decomposition, and promotes the formation of a dense, stable oxide layer consisting primarily of Al₂O₃ and Ta₂O₅. From a physical standpoint, these improvements are attributed to the larger ionic radius of Ta⁵⁺, its electronic configuration, solid solution strengthening effects, grain refinement, and the formation of stronger Ta-N bonds [9-13]. Moreover, Ta addition reduces the mixing enthalpy and stabilizes rutile-type TiO₂ structures under oxidizing conditions. These effects result in a significant increase in both hardness and oxidation resistance of the coating. All the insights have been possible thanks to extensive studies, particularly from groups at TU Wien [6,9,12-14] and Montanuniversität Leoben [11]. Since the first patent in 2005 [15], the TiAlTaN system has been investigated through various experimental and computational approaches. Key advancements include optimization of Ta content, already identified in 2008 to be between 10 and 20at. %, and the use of density functional theory (DFT) to study phase stability and bonding energetics. Multilayered structures and advanced studies of oxidation mechanisms have further refined the understanding of tantalum role in these coatings [13,14,16]. In 2022, Hemmati et al. [10] reported a comparative study of monolithic TiAlTaN coatings, multilayer TiAlTaN/TiAlN coatings, and multilayer TiAlTaN/TiAlTaN coatings with alternating the bias, including cutting tests, and compared with TiAlN. Their XRD analysis confirmed the delayed spinodal decomposition, with differences between monolayer and multilayer TiAlTaN coatings. Monolayer TiAlTaN showed superior oxidation resistance, while Ta-free multilayers fully oxidized after 20 h at 1000 °C. In machining tests, monolayer TiAlTaN extended tool life by ~25% over TiAIN, mainly due to delayed crater wear and reduced substrate exposure. This improvement is linked to the formation of protective tribo-oxide layers, which also enhanced chip flow and metal deformation at the chip-tool interface. The cutting performance of TiAlTaN coatings has also been rarely addressed in previous studies. A recent study from Tillman et al. [17] reported that the higher performance of TiAlTaN (and TiAlSiN) for micromilling, compared to TiAlN.

Despite this wealth of research, many studies to date have been based on arc deposition techniques. High Power Impulse Magnetron Sputtering (HiPIMS), known for producing dense films with tailored microstructures, from highly ionized but droplet-free discharge, remains largely unexplored for TiAlTaN coatings. HiPIMS offers potential advantages in terms of film density, adhesion, level of defect and property control, factors that are particularly relevant for cutting tool applications. More precisely, HiPIMS has a significant advantage over cathodic arc for very sharp tools (microdrill, cutting blades), where defects and high roughness may dramatically affect the tool performances. In 2024, Lopes Dias et al. [8] presented a complete study, comparing the use of DC, HiPIMS and hybrid DC/HiPIMS process

to produce TiAlTaN coatings. The use of the hybrid process shows a good compromise to mitigate the decrease of deposition rate, while keeping excellent mechanical properties.

In the present work, we present a comprehensive investigation of TiAlTaN coatings deposited by HiPIMS with various Ta content. The study integrates experimental characterization, kinetic Monte Carlo simulations, and cutting performance tests. We aim to elucidate the correlation between deposition conditions, microstructure, and mechanical/thermal properties and cutting performances. Our results offer new insights into the design and application of advanced nitrides for high-performance machining. The main novelty of the work lies in complete approach, with the determination of physicochemical and mechanical properties that are linked with cutting performance and results from simulation.

Materials and methods

 $Ti_xAI_{1-x}Ta_yN$ coatings have been deposited in a hexagonal, semi-industrial chamber (D&M Vacuumsystemen) with an approximate volume of 1 m³. The chamber design and geometry are described elsewhere in [4,18]. It is equipped with rectangular $Ti_{50}AI_{50}$, $Ti_{45}AI_{45}Ta_{10}$ or $Ti_{40}AI_{40}Ta_{20}$ targets (7.5 cm × 35 cm, 99.9% purity, Plansee Composite Materials GmbH). The composition of the target, namely 45/45/10 and 40/40/20 is used for the identification of samples: $TiAITaN \ 45/45/10$ and 40/40/20 samples are respectively synthesized samples from the corresponding targets. Targets have been sputtered in HiPIMS mode, with t_{ON} and t_{OFF} of 50 and 1950µs respectively (duty cycle of 2.5%, frequency 500Hz), with current regulation of 1.5A, in Ar/N_2 atmosphere (150sccm of Ar and 120 sccm of N_2), with a bias voltage of 150V, at a pressure of 1.3 Pa (10 mTorr). It corresponds to an average power of 1.3 and 1kW for TiAITaN and TiAIN coating respectively and a peak power density of 698, 637 and 664 W.cm⁻² for TiAIN, TiAITaN 45/45/10 and 40/40/20 respectively (considering the full size of the target; the racetrack represent $\approx 30\%$ of the target surface). DC sputtering has also been used with similar configuration and different deposition time, from 2 to 6h, for few endmills. No additional heating is used for deposition.

Multiple substrates have been used: Si substrates, ultrasonically cleaned prior to deposition in ethanol, but also stainless steel (AISI 316L, 20x20x2mm), HSS (HSSCo8, HOFFMAN) and cemented carbide endmills (Ø6mm, 6% Co, MGR Herstal). Metallic substrates have been cleaned using a standard and established procedure, including Vakukleen and Galvex 18.08 products (NGL Cleaning Technology SA), with hot air drying. AISI 316L susbtrate has been used for XRD, XPS and nanoindentation analysis. All samples were mounted on a table with three-fold planetary rotation at 5 RPM. Before deposition, the chamber is evacuated to a base pressure below 6.7×10^{-3} Pa $(5.0 \times 10^{-6}$ Torr), and substrates undergo plasma etching in pure Ar at 3.33 Pa (25 mTorr) and -600V, during 10min. It is important to mention that this work gathers numerous different coatings, deposited in similar conditions, but with various deposition time. This is the reason that several thicknesses are obtained for cutting tests. The deposition rate is also different for endmills and Si or stainless-steel coupons, as the radius of rotation differs. Compared to pure TiAIN, the deposition rate of TiAITa 45/45/10 and 40/40/20 are respectively +61% and +64% for the same deposition condition.

Following the deposition, stainless steel coated samples have undergone annealing in air (Carbolite Gero CWF 1100, 30–1100 °C) at temperatures ranging from 600 °C to 800 °C, for 2h. Hardness measurements have been performed using a nanoindenter (Fischerscope HM2000 S, Fischer Instrumentation Électronique) with a Berkovich tip, following the Oliver and Pharr method [19]. The crystallinity of the samples has been analysed via X-ray diffraction (X'Pert PRO, Panalytical, Netherlands) in $\theta/2\theta$ configuration, using a monochromatic Cu K α X-ray source (λ = 1.5406 Å).

Elemental depth profiles are obtained through X-ray Photoelectron Spectroscopy (XPS, K-Alpha, Thermo Scientific), employing a monochromatic Al K_{α} source working at 1486.68 eV. The spot and raster sizes are set to 250 μ m \times 250 μ m and 1.25 mm \times 1.25 mm, respectively. To obtain composition depth profiles, sputtering of the coated surface was conducted with a 2 keV monoatomic Ar⁺ beam at a 30° incidence angle. Core levels Ti 2p, N 1s, O 1s, Al 2p, C 1s, Ta 4f, and Fe 2p (or Si 2p depending on the substrate) are recorded in snap mode over 20 scans. Ta 4f is preferred rather than Ta4p as it slightly overlaps N 1s signal. The N1s signal has been carefully fitted along with Ta4p signal, to avoid overquantification of nitrogen. For composition depth profiling, peak areas were analyzed using a Shirley background subtraction and peak with L/G ratio of 30. The authors acknowledge recent literature addressing concerns about XPS on insulating materials and potential problematic calibration and peak fitting [20–22]. Here, a flood gun has been used, the position of valence band has been checked, and the peak shifts are not discussed (only the quantification).

Machining tests have also been performed with coated and uncoated endmills. For this purpose, a Kunzmann WF 610 MC milling machine has been used, where the spindle power is recorded during machining tests. 3-teeth HSS and cemented carbide endmills of Ø6mm were mounted on the spindle, with cutting depth of 3mm. The cutting speed V_c and feed rate F are respectively of 37m/min and 60mm/min, namely a speed per tooth F_z of 0.01mm. The workpiece is a cylinder of quenched 42CrMo4 steel (38HRC), where a groove of 20cm is machined, without lubrication. Such conditions are voluntarily extreme to avoid too long machining tests, while being comparative.

To complement the machining tests, kinetic Monte Carlo (k-MC) simulations were performed using VirtualCoater[™] (ICS – Innovative coating solutions S.A.), in order to elucidate the influence of deposition conditions and composition on the coating's growth mechanism. Both DC and HiPIMS discharges are simulated, and a fraction of 30% of ionized species is considered for HiPIMS deposition. This level is chosen from [23] and considering the relatively low peak power density used here. A computational time of 30min is needed, for 1000 steps of deposition to carefully represent the 3-fold rotation of the substrates.

Results and discussion

Figure 1 presents the evolution of the hardness of three coatings after deposition (thickness about $1\mu m$), and after annealing in air during 2h, at 600, 700 and 800°C. The TiAlN coating has a hardness of 20GPa, while the addition of Ta increases the hardness to 32.6 and 35.8GPa for TiAlTaN 45/45/10 and 40/40/20, respectively. These values agree with hardness measurements from Lopes Dias et al. and other studies [8,12]. It is important to mention that for some deposition conditions (different duty cycle, bias, magnetic configuration), higher hardness up to 45GPa have been achieved. For TiAlN coating, the hardness is rather low compared to traditional values (in the range of 25-33GPa), with values of 34GPa reported in the same coater in bipolar dual magnetron sputtering [4]. This is attributed to the low crystallinity of the coating (see XRD section). After annealing, a considerable drop of the hardness is reported, below 20GPa. This is due to the formation of an oxide layer formation on the top of the films, as the indentation depth is similar to oxide thickness. These values correspond to the hardness of alumina [24]. The hardness tends to increase for Ta doped films with annealing at 800°C, which might be due to age hardening effect, which are not seen on TiAlN, as it decomposed into wurtzite (see below).

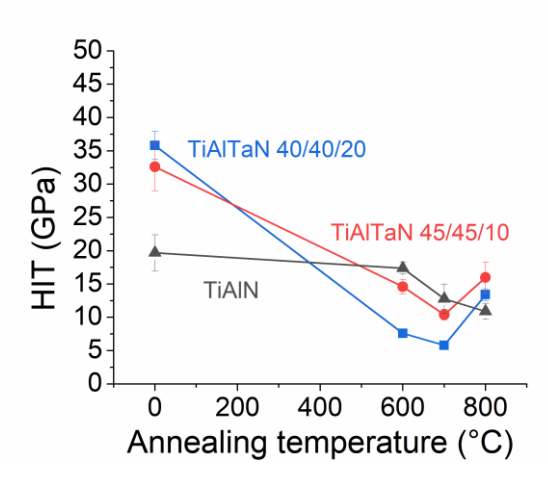


Figure 1. Evolution of penetration hardness HIT as a function of different annealing temperature in air, during 2h, for TiAlN, TiAlTaN 45/45/10 and TiAlTaN 40/40/20 films

The evolution of the structure of the films after annealing is presented on Figure 2. For TiAIN coatings (Figure 2.a), the as-deposited films exhibit a cubic structure, with a (111) diffraction peak appearing at 35.5°. This value is largely shifted toward smaller angles compared to usual values reported of TiAIN coating (around 36.5-37°), with Al/Ti ratio close to 1 [4,25]. The crystallinity of the film is low, with very weak peak intensity. We do not have specific explanation for this intriguing result, which agrees with the low hardness reported. No significant change occurs up to 800°C where the decomposition of cubic phase into hexagonal phase starts (meaning that spinodal decomposition occurs for an intermediate time/temperature annealing condition), with new diffraction peaks at 33.3, 35.7 and 36.9°, corresponding to (100), (002) and (101) directions. For TiAlTaN 45/45/10 and 40/40/20 coatings (Figure 2 b and c), a strong preferential orientation is evidenced with the (111) diffraction peak at 36.3 and 36.1° respectively, therefore, slightly shifted toward literature values of (111) TiAIN diffraction peak (36.5-37°). This is in agreement with the larger lattice parameter, due to the larger atomic size of Ta, expanding the lattice. A second peak at 60.8° and 60.6° is also visible corresponding to (220) plane. Annealing at 600°C in air during 2h causes the diffraction peaks to shift toward higher angles, indicating a reduction in lattice parameter due to the thermal relaxation of compressive stresses. For TiAlTaN 45/45/10, the structure remains unchanged up to 2h at 800°C, indicating the high stability of this composition. For TiAlTaN 40/40/20, the spinodal decomposition into two cubic structures is noticed, with a shoulder appearing at 36.1° and a new peak at 62.4°. One can also notice a small peak at around 69° after annealing at 800°C during 2h, that is not clearly identified. In case of crystalline oxide formation, more peaks should be seen on 30-40° range. These measurements confirm (1) the decomposition of c-TiAlN into wurtzite, (2) the high stability of TiAlTaN 45/45/10 structure, and (3) the too large content of Ta in TiAlTaN 40/40/20 coating promoting the spinodal decomposition.

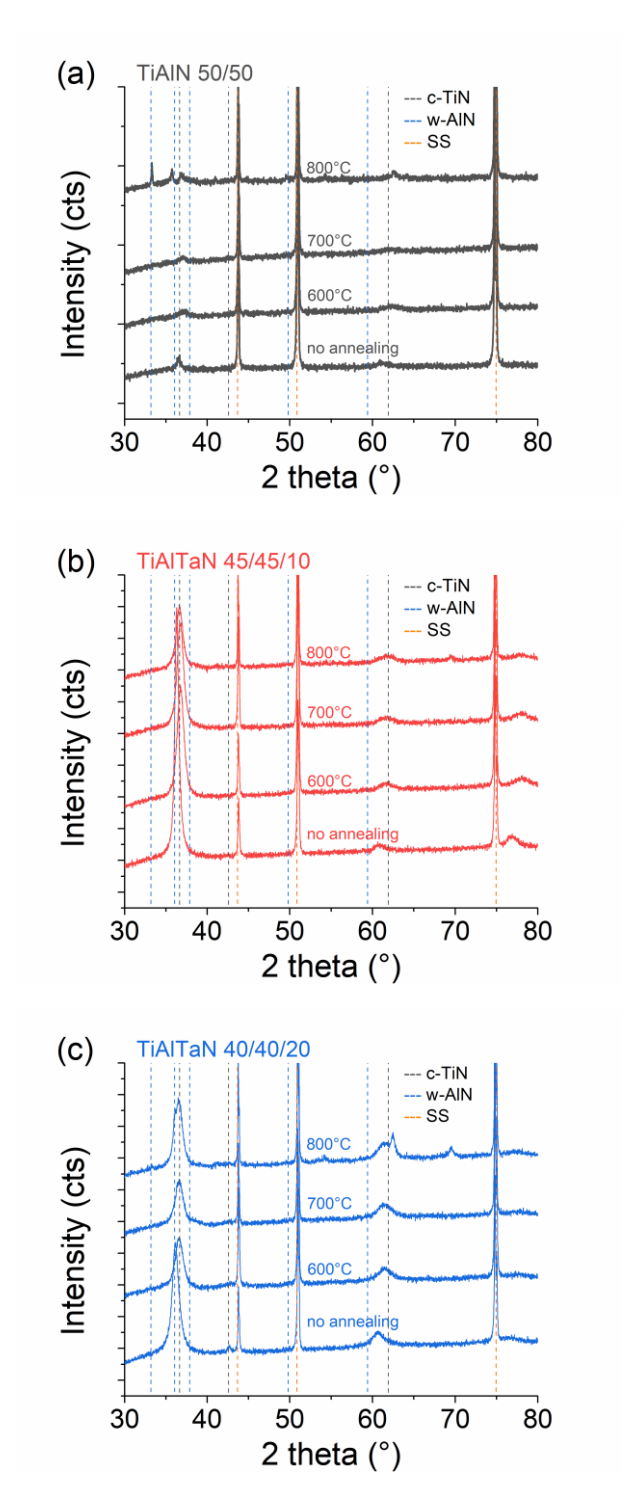


Figure 2. Evolution of XRD patterns of (a) TiAlN, (b) TiAlTaN 45/45/10 and (c) TiAlTaN 40/40/20 as deposited and after annealing in air at 600, 700 and 800°C during 2h. SS signal (in orange) corresponds to stainless steel substrate.

Figure 3 presents the XPS depth profiles of TiAlN, TiAlTaN 45/45/10 and TiAlTaN 40/40/20 before and after annealing in air at 600, 700 and 800°C. All as-deposited films contain 3-10at% of oxygen, a typical contamination reported for nitride coatings deposited in these conditions, especially in this coater [4,18,26,27]. The working current was rather low (1.5A), explaining this relatively high oxygen contamination. A larger oxygen contamination for the TiAlTaN 40/40/20 coating is noticed. The TiAlTaN

45/45/10 and TiAlTaN 40/40/20 respectively contain 8 and 12at% of Ta. The Table 1 presents the composition and x and y fraction (excluding oxygen presence) for the sake of clarity.

Table 1. Relation between target composition and film composition, and corresponding fraction of element for conventional $Ti_xAI_{1-x}Ta_vN$.

Ti/Al/Ta target	Derived film composition (at.%) from XPS				Approximate x and y fraction	
composition	Ti	Al	Та	N	0	considering Ti _x Al _{1-x} Ta _y N and no O
50/50/0	24	25	0	42	8	x=0.5, y=0 Ti _{0.5} Al _{0.5} N
45/45/10	23	22	8	40	7	x=0.42, y=0.16 Ti _{0.42} Al _{0.42} Ta _{0.16} N
40/40/20	20	20	12	38	10	x=0.42, y=0.16 Ti _{0.38} Al _{0.38} Ta _{0.23} N

After annealing in air during 2h at 600°C (Figure 3.b, f, j) all film present a mixed oxide layer, which is in agreement with type-2 oxidation behavior, namely, no Al diffusion to the surface, as described by Greczynski *et al.*[5]. After annealing at 800°C, the TiAlN coating switch to type 1 oxidation, with the formation of bilayer, with Al_2O_3 on the top and TiO_2 underlayer, due to active diffusion of Al. Again, these results perfectly match the predictive maps reported in [5].

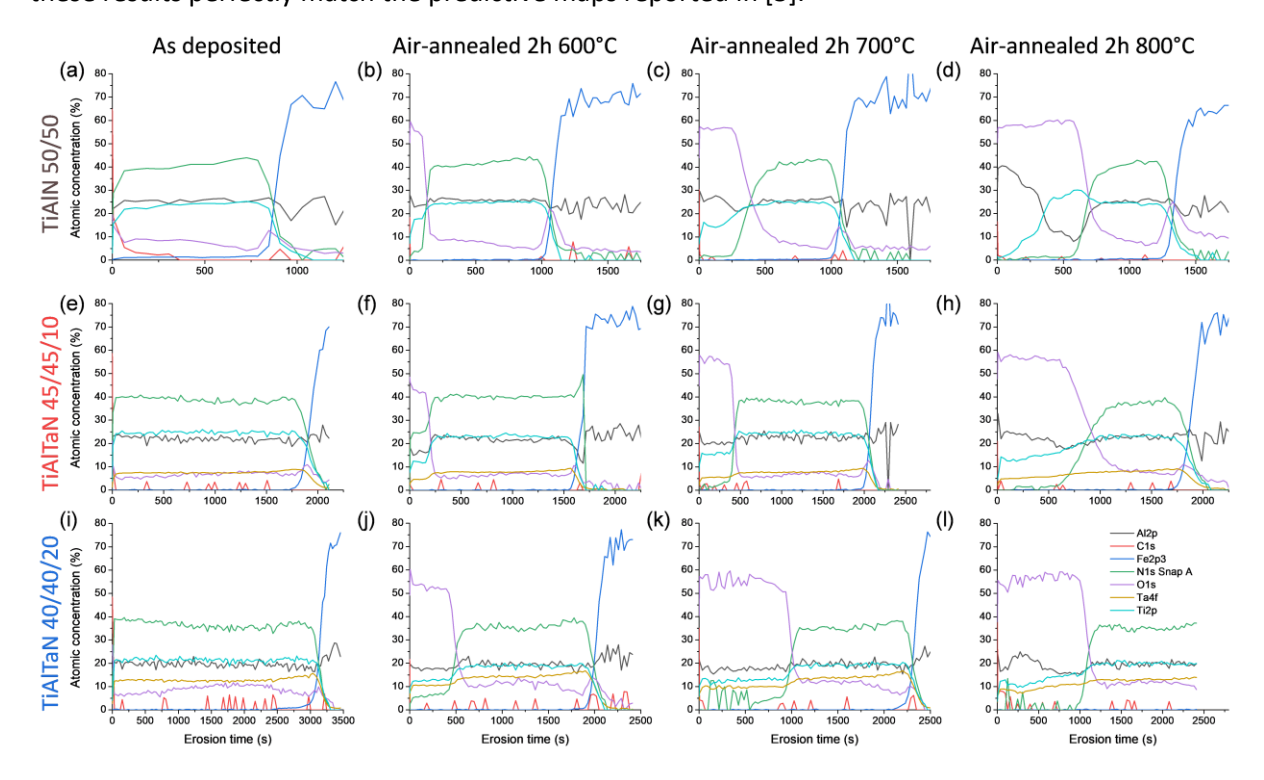


Figure 3. XPS depth profiles of (a-d) TiAlN, (e-h) TiAlTaN 45/45/10 and (i-l) TiAlTaN 40/40/20 after deposition and after annealing in air at 600, 700 and 800°C during 2h.

Interestingly, TiAlTaN 45/45/10 and TiAlTaN 40/40/20 exhibit a different behavior, with the formation of a mixed oxide layer, containing Ti, Al and Ta. For TiAlTaN 40/40/20, one can notice the slight enrichment of Al close to the surface, possibly indicating the beginning of type 1 oxidation. These results also confirm the optimal concentration for the 45/45/10 composition for a better oxidation resistance. The difference in terms of oxidation behavior is further confirmed by SEM analysis (Figure 4): the figure presents the SEM cross section of the coating, before and after air-annealing at 800°C during 2h. All cross sections are made on stainless-steel coated substrates, except on as-deposited TiAlN samples (Figure 4.a), where Si substrate is used. One can first see the increase of the thickness (for the same deposition time) when higher Ta content is used (Figure 4 a, c, e). Moreover, morphology

tends also to evolve with dense coating for TiAlN, fine granular morphology for TiAlTaN 45/45/10 and close-pack fibrous film for TiAlTaN 40/40/20. After annealing, the thinnest oxide layer is obtained for TiAlTaN 45/45/10 coating, with the formation of dense (TiAlTa)O_x monolayer of \approx 80nm, while a similar but thicker (TiAlTa)O_x monolayer of \approx 310nm obtained for TiAlTaN 40/40/20 coating. For TiAlN, one can clearly observe the formation of bilayer with a total thickness of \approx 340nm, containing a porous sublayer of TiO₂ below the Al₂O₃ top layer.

One can notice that for annealing at 800°C, the sputtering time for TiAlN on XPS depth profile was significantly shorter, and therefore, could indicate better oxidation resistance. However, on SEM pictures (Figure 4.b), it is clear that the thickness of the oxide layer the largest. This comes from the higher sputtering rate of the porous oxide during on the oxidized TiAlN sample during XPS depth profiling, compared to Ta-containing samples where a denser oxide layer is formed.

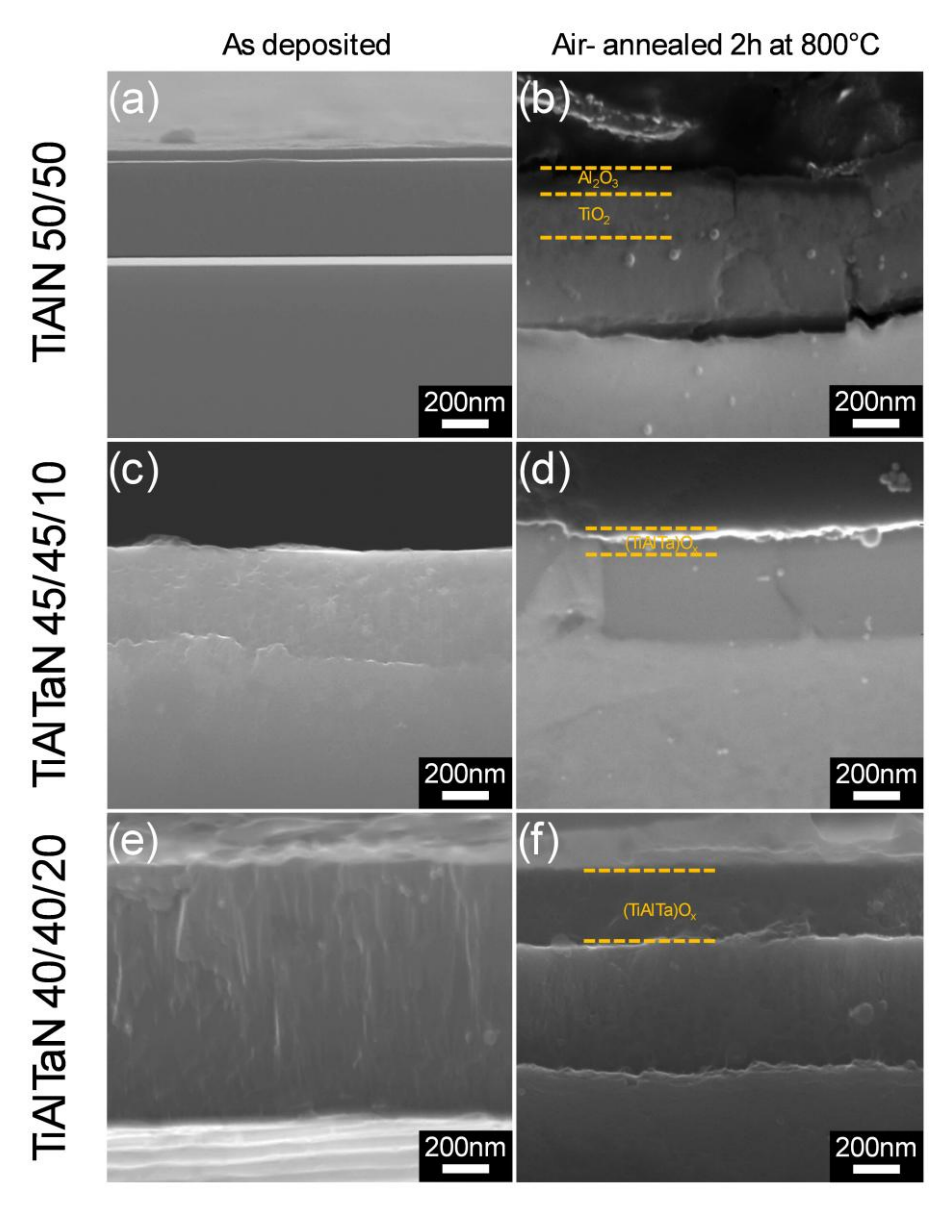


Figure 4. SEM cross section of TiAIN, TiAITaN 45/45/10 and TiAIN 40/40/20 before (a,c,e) and after air-annealing at 800°C during 2h (b,d,e). All cross sections are made on stainless substrate, expect (a), where Si substrate is used.

In addition to these physico-chemical characterizations, comparative machining tests have been performed using a Kunzmann WF 610 MC milling machine (Figure 5). It consists of the dry machining of 42CrMo4 steel, with a groove distance of 20cm and a cutting depth of 3mm, without any lubrication (Figure 5.b). The other cutting parameters are given in the insert of Figure 5.a. The in-situ spindle power (Pelec) is recorded during the test. It is assumed that a higher spindled power implies higher friction during machining. A power of 600W is requested for the tool rotation, corresponding to the baseline. An uncoated HSS endmill fails around 320s, and an electrical power of 720W is needed. Each drop and rise correspond to the beginning and end of each groove. Different HSS coated tools have been tested, including TiAlN, TiAlTaN 45/45/10 and TiAlTaN 40/40/20 synthesized using HiPIMS, but also TiAlTaN 40/40/20 synthesized using DC sputtering. The TiAIN done by HiPIMS fails before 500s, which is attributed to the lower hardness of the coating, but also its lower thickness in this case. The TiAlTaN 40/40/20 composition performs better, with lower electrical consumption, and longer lifetime. The effect of thickness seems to be predominant over the discharge mode, as the TiAlTaN 40/40/20 synthesized by HiPIMS, with thickness of 1µm fails around 1400s, while the lifetime is extended up to 1750s using DC mode and thickness of 1.4µm. The coating exhibiting the better cutting performance is again the TiAlTaN 45/45/10 synthesized by HiPIMS, which is able to withstand 2500s with an initial electrical power of 630W that ends up stabilizing around 700W, even with a thickness of 1µm. These machining tests confirm the physico-chemical characterizations (hardness, structure, composition) where a performance optimum is reached for a Ta content of 8at.%.

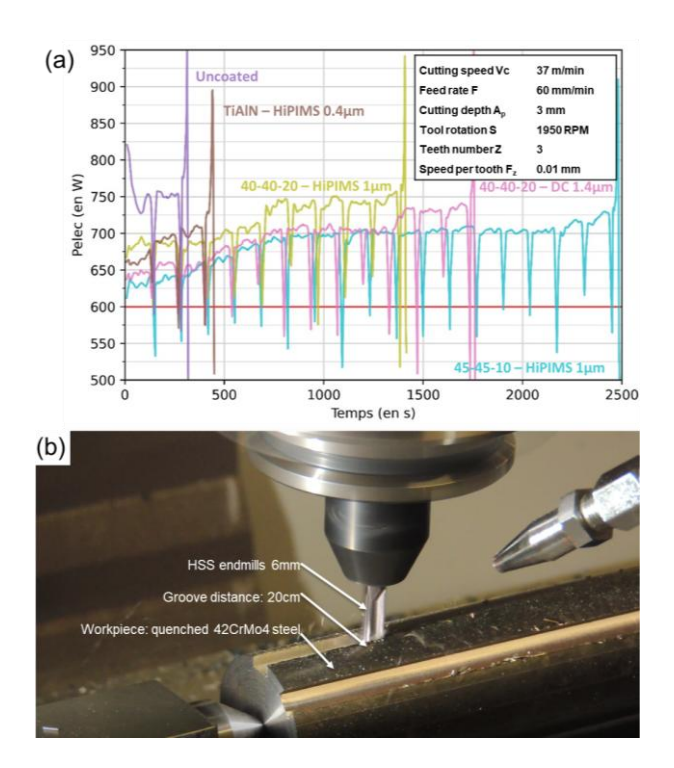


Figure 5. (a) evolution of the in-situ spindle power during machining of 42CrMo4 workpiece with different HSS endmills, as a function of time and (b) setup used for machining. The inset in (a) reports the cutting parameters. The baseline in red at 600W corresponds to the electrical power for rotation without any machining.

Interestingly, the "optimal" Ta content of 8at.% obtained in this work for cutting performance, hardness and oxidation resistance (which is obviously not fully optimized as it would require additional tests with different compositions), namely a Ta metal fraction of y=0.16 (for $Ti_xAI_{1-x}Ta_yN$, with x+y=1), is close to

the value of 0.12 recently reported by Lopes Dias et al. [8]. For this Ta fraction, the primary factors contributing to the improved properties are: (i) solid solution strengthening from the incorporation of Ta atoms into the lattice, (ii) increased compressive stresses, and (iii) enhanced cohesive strength due to a higher valence electron concentration [8,28]. However, the value reported by Lopes Dias et al. at 0.12 was already lower than values $0.20 \le y \le 0.37$ previously reported in [7,29,30]. Looking more in details in these publications, the optimum seems to shift to lower values in correlation with the choice of the discharge: Sui et al. reported the use of RF and DC sputtering of TiAl and Ta targets, with optimum at y=0.37, while Shugurov's optimum is at 0.35, also with DC reactive sputtering of TiAl and Ta targets. Lopes Dias et al. reported optimum at y=0.18 for DC and hybrid DC/HiPIMS and 0.12 for pure HiPIMS, with a frequency of 940Hz and a duty cycle of 5.6%, and average power density of 13W/cm². Our work reports an optimum at y=0.16 for a frequency of 500Hz at 2.5% duty cycle, with an average power density of 5W/cm² and peak power density ≈640W/cm². It is well established that the peak power density is one of driving factor to control the metal ion fraction, that will then drive the mechanical properties of the film [18,31,32]. This is also the basis of the concept for the positive kick after negative pulse to push ions toward the substrate [33,34]. Even other parameters are of high importance (such as magnetic configuration or pressure/distance ratio), this shift of Ta content optimum is attributed to proportion of metallic ions that increase from DC to hybrid DC/HiPIMS to pure HiPIMS. An optimum is found, as a too high Ta content will promote new phase, excessive compressive stress, and abnormal grain growth. Further plasma diagnostics and additional data from the literature are required to clearly correlate the ionized metal fraction, the Ta content, and the mechanical properties.

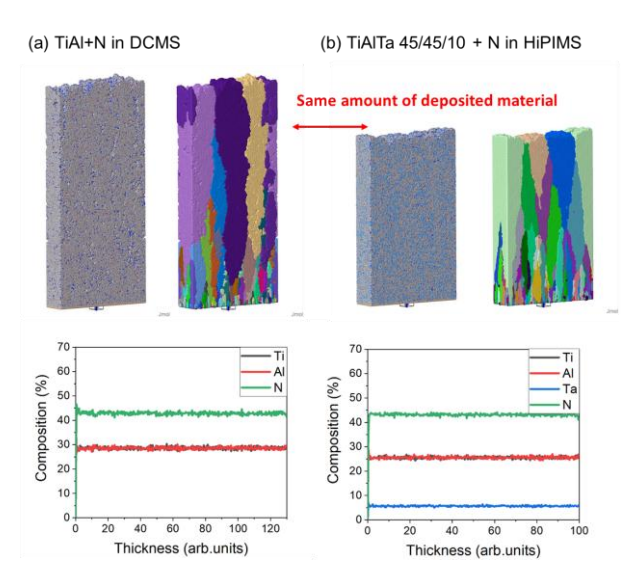


Figure 6. VirtualCoater[™] simulation of TiAlN and TiAlTaN 45/45/10 coating deposited respectively in DC and HiPIMS mode, and corresponding composition profile extracted from the simulation.

To better understand the role of Ta in film growth, kMC simulations have been performed using VirtualCoaterTM software. The Figure 6 presents the results of thin film growth simulations of TiAl sputtered in Ar and N_2 in DC mode (Figure 6.a) and TiAlTa 45/45/10 sputtered in in Ar and N_2 HiPIMS mode, considering an ionized fraction of 30%. The same amount of material is deposited in both cases (3.2x10⁶ atoms), while the substrate dimensions are 200 x 50 atoms. Thus, the thickness of simulated coatings are about 320 atomic layers, which corresponds to about 100 nm. It is necessary to mention, that real thickness of simulated coatings are higher as the coatings are not fully dense and contains from 10% to 25% percent of voids. The corresponding visualization with column detection is also reported, in addition to composition profile extracted from the simulation. First, the thickness decreases significantly, due to densification process from ionic bombardment. The reported density,

extracted from the simulation are respectively equal to 75 and 90% of the bulk density for TiAIN and TiAITaN 45/45/10. The composition profile almost matches well the XPS depth profiles (Figure 3.a&e), with a Ta content of 6at. % for TiAITaN 45/45/10. This is slightly less, than the Ta content measured experimentally. One of a possible explanation of the difference is that in the simulations it is assumed that sticking coefficient for all species, Ti, Al, and Ta are the same. Still, the sticking coefficients for different species may be different, causing the difference. Less porosity in the film is also reported, and a drop of the roughness is also noticed. Thanks to a dedicated plugin (which use a virtual probe to measure the z direction, like AFM measurement), the roughness decreases from 10 to 4.75 atomic units. We measure the RMS roughness in atomic units, or average diameter of an atom as the simulations are performed at atomic scale, thus this is a natural unit for the case. This drop of roughness, concomitant to the higher density are responsible for the better cutting performance [35]. The k-MC simulations provide therefore a mechanistic understanding of the superior machining behavior of TiAITaN 45/45/10. The predicted higher density and smoother morphology are consistent with the experimental results, indicating that the improved coating microstructure (as seen in SEM also) contributes to enhanced tool life and surface finish.

Conclusion

TiAlN and TiAlTaN coatings were successfully synthesized by HiPIMS using TiAl and TiAlTa targets with compositions of 40/40/20 and 45/45/10, respectively. The optimal performance was observed for the TiAlTaN coating derived from the 45/45/10 target, corresponding to a Ta metal fraction of 0.16. The incorporation of Ta into the TiAlN matrix significantly enhances both hardness and oxidation resistance. These improvements are attributed to solid solution strengthening, grain refinement, and the formation of a stable, protective mixed oxide layer. Simulation results further corroborate experimental findings, indicating increased coating density and reduced surface roughness. Compared to conventional cathodic arc deposition, the HiPIMS process yields smoother and denser coatings due to droplet free process, making TiAlTaN deposited by HiPIMS a promising candidate for advanced protective applications requiring high mechanical performance and thermal stability.

Declaration of generative AI in scientific writing

During the preparation of this work the authors used ChatGPT in order to help in the preparation of the introduction section. After using this tool/service, the authors reviewed and edited the content as needed and take full responsibility for the content of the published article.

Declaration of competing interest

Acknowledgment

E.H. and S.L. acknowledge the SPW (Service Public de Wallonie) for the funding of the TINALTA project (convention n° 1910092). The Synthesis, Irradiation & Analysis of Materials (SIAM), Physico-Chemical Characterization (PC2), and Morph'IM platforms of the University of Namur are acknowledged for XPS, XRD, and SEM facilities. S.L., J.M. and P.M. acknowledge the financial support from the European Commission for conducting the research and technological developments in the EU Horizon Europe M2DESCO Project (EU Grant Agreement number 101138397).

References

- [1] T. Leyendecker, O. Lemmer, S. Esser, J. Ebberink, The development of the PVD coating TiAlN as a commercial coating for cutting tools, Surface and Coatings Technology 48 (1991) 175–178. https://doi.org/10.1016/0257-8972(91)90142-J.
- [2] R. Rachbauer, J.J. Gengler, A.A. Voevodin, K. Resch, P.H. Mayrhofer, Temperature driven evolution of thermal, electrical, and optical properties of Ti–Al–N coatings, Acta Materialia 60 (2012) 2091–2096. https://doi.org/10.1016/j.actamat.2012.01.005.
- [3] M. Bartosik, C. Rumeau, R. Hahn, Z.L. Zhang, P.H. Mayrhofer, Fracture toughness and structural evolution in the TiAlN system upon annealing, Sci Rep 7 (2017) 16476. https://doi.org/10.1038/s41598-017-16751-1.
- [4] L. Chavee, E. Serag, M. da Silva Pires, S. Lucas, E. Haye, A mechanistic approach of oxidation resistance, structural and mechanical behaviour of TiAlN coatings, Applied Surface Science 586 (2022) 152851. https://doi.org/10.1016/j.apsusc.2022.152851.
- [5] G. Greczynski, L. Hultman, M. Odén, X-ray photoelectron spectroscopy studies of Ti1-xAlxN ($0 \le x \le 0.83$) high-temperature oxidation: The crucial role of Al concentration, Surface and Coatings Technology 374 (2019) 923–934. https://doi.org/10.1016/j.surfcoat.2019.06.081.
- [6] C.M. Koller, R. Hollerweger, C. Sabitzer, R. Rachbauer, S. Kolozsvári, J. Paulitsch, P.H. Mayrhofer, Thermal stability and oxidation resistance of arc evaporated TiAlN, TaAlN, TiAlTaN, and TiAlN/TaAlN coatings, Surface and Coatings Technology 259 (2014) 599–607. https://doi.org/10.1016/j.surfcoat.2014.10.024.
- [7] X. Sui, G. Li, C. Jiang, H. Yu, K. Wang, Q. Wang, Effect of Ta content on microstructure, hardness and oxidation resistance of TiAlTaN coatings, International Journal of Refractory Metals and Hard Materials 58 (2016) 152–156. https://doi.org/10.1016/j.ijrmhm.2016.04.014.
- [8] N.F. Lopes Dias, A.L. Meijer, D. Biermann, W. Tillmann, Structure and mechanical properties of TiAlTaN thin films deposited by dcMS, HiPIMS, and hybrid dcMS/HiPIMS, Surface and Coatings Technology 487 (2024) 130987. https://doi.org/10.1016/j.surfcoat.2024.130987.
- [9] R. Hollerweger, H. Riedl, J. Paulitsch, M. Arndt, R. Rachbauer, P. Polcik, S. Primig, P.H. Mayrhofer, Origin of high temperature oxidation resistance of Ti–Al–Ta–N coatings, Surface and Coatings Technology 257 (2014) 78–86. https://doi.org/10.1016/j.surfcoat.2014.02.067.
- [10] A. Hemmati, M. Abdoos, S.C. Veldhuis, Developing Ti-Al-Ta-N based coatings: Thermal stability, oxidation resistance, machining performance and adaptive behavior under extreme tribological conditions, Materials Today Communications 31 (2022) 103373. https://doi.org/10.1016/j.mtcomm.2022.103373.
- [11] B. Grossmann, M. Tkadletz, N. Schalk, C. Czettl, M. Pohler, C. Mitterer, High-temperature tribology and oxidation of Ti1–x–yAlxTayN hard coatings, Surface and Coatings Technology 342 (2018) 190–197. https://doi.org/10.1016/j.surfcoat.2018.02.062.
- [12] W.M. Seidl, M. Bartosik, S. Kolozsvári, H. Bolvardi, P.H. Mayrhofer, Improved mechanical properties, thermal stabilities, and oxidation resistance of arc evaporated Ti-Al-N coatings through alloying with Ta, Surface and Coatings Technology 344 (2018) 244–249. https://doi.org/10.1016/j.surfcoat.2018.03.014.
- [13] W.M. Seidl, M. Bartosik, S. Kolozsvári, H. Bolvardi, P.H. Mayrhofer, Mechanical properties and oxidation resistance of Al-Cr-N/Ti-Al-Ta-N multilayer coatings, Surface and Coatings Technology 347 (2018) 427–433. https://doi.org/10.1016/j.surfcoat.2018.05.025.
- [14] Y. Yang, Y.X. Xu, L. Chen, P.H. Mayrhofer, Improved Ti-Al-N coatings through Ta alloying and multilayer architecture, Surface and Coatings Technology 328 (2017) 428–435. https://doi.org/10.1016/j.surfcoat.2017.09.016.
- [15] M. Kathrein, C. Michotte, P. Polcik, Beschichtetes werkzeug, AT8346U1, 2006. https://patents.google.com/patent/AT8346U1/en?oq=EP1726687 (accessed August 18, 2025).
- [16] X. Sui, G. Li, C. Jiang, Y. Gao, K. Wang, Q. Wang, Improved surface quality of layered architecture TiAlTaN/Ta coatings for high precision micromachining, Surface and Coatings Technology 320 (2017) 298–303. https://doi.org/10.1016/j.surfcoat.2016.12.083.

- [17] W. Tillmann, A.L. Meijer, T. Platt, D. Biermann, D. Stangier, N.F. Lopes Dias, Cutting performance of TiAlN-based thin films in micromilling high-speed steel AISI M3:2, Manufacturing Letters 40 (2024) 6–10. https://doi.org/10.1016/j.mfglet.2024.01.005.
- [18] E. Haye, J.L. Colaux, P. Moskovkin, J.-J. Pireaux, S. Lucas, Wide range investigation of duty cycle and frequency effects on bipolar magnetron sputtering of chromium nitride, Surf. Coat. Technol. 350 (2018) 84–94. https://doi.org/10.1016/j.surfcoat.2018.07.009.
- [19] G.M. Pharr, W.C. Oliver, Measurement of Thin Film Mechanical Properties Using Nanoindentation, MRS Bull. 17 (1992) 28–33. https://doi.org/10.1557/S0883769400041634.
- [20] G. Greczynski, L. Hultman, Compromising Science by Ignorant Instrument Calibration—Need to Revisit Half a Century of Published XPS Data, Angewandte Chemie International Edition 59 (2020) 5002–5006. https://doi.org/10.1002/anie.201916000.
- [21] G. Greczynski, L. Hultman, X-ray photoelectron spectroscopy: Towards reliable binding energy referencing, Progress in Materials Science 107 (2020) 100591. https://doi.org/10.1016/j.pmatsci.2019.100591.
- [22] J.W. Pinder, G.H. Major, D.R. Baer, J. Terry, J.E. Whitten, J. Čechal, J.D. Crossman, A.J. Lizarbe, S. Jafari, C.D. Easton, J. Baltrusaitis, M.A. van Spronsen, M.R. Linford, Avoiding common errors in X-ray photoelectron spectroscopy data collection and analysis, and properly reporting instrument parameters, Applied Surface Science Advances 19 (2024) 100534. https://doi.org/10.1016/j.apsadv.2023.100534.
- [23] L. Zauner, A. Bahr, T. Kozák, J. Čapek, T. Wojcik, O. Hunold, S. Kolozsvári, P. Zeman, P.H. Mayrhofer, H. Riedl, Time-averaged and time-resolved ion fluxes related to reactive HiPIMS deposition of Ti-Al-N films, Surface and Coatings Technology 424 (2021) 127638. https://doi.org/10.1016/j.surfcoat.2021.127638.
- [24] Q. Li, Y.-H. Yu, C. Singh Bhatia, L.D. Marks, S.C. Lee, Y.W. Chung, Low-temperature magnetron sputter-deposition, hardness, and electrical resistivity of amorphous and crystalline alumina thin films, Journal of Vacuum Science & Technology A 18 (2000) 2333–2338. https://doi.org/10.1116/1.1286715.
- [25] A. Mendez, M.A. Monclus, J.A. Santiago, I. Fernandez-Martinez, T.C. Rojas, J. Garcia-Molleja, M. Avella, N. Dams, M. Panizo-Laiz, J.M. Molina-Aldareguia, Effect of Al content on the hardness and thermal stability study of AlTiN and AlTiBN coatings deposited by HiPIMS, Surface and Coatings Technology 422 (2021) 127513. https://doi.org/10.1016/j.surfcoat.2021.127513.
- [26] E. Serag, E. Haye, B. Caers, P. Schuurmans, S. Lucas, Changes in chemical composition of TixAl1-xN coatings immersed in oxygen-saturated Lead-Bismuth Eutectic at low and moderate temperatures (250 °C \le T \le 410 °C), Progress in Nuclear Energy 172 (2024) 105217. https://doi.org/10.1016/j.pnucene.2024.105217.
- [27] E. Serag, B. Caers, E. Haye, P. Schuurmans, S. Lucas, Revealing wear mechanisms of coated shafts in low-speed journal bearings immersed in liquid Lead-Bismuth Eutectic (LBE), Tribology International 201 (2025) 110264. https://doi.org/10.1016/j.triboint.2024.110264.
- [28] W.M. Seidl, M. Bartosik, S. Kolozsvári, H. Bolvardi, P.H. Mayrhofer, Influence of Ta on the fracture toughness of arc evaporated Ti-Al-N, Vacuum 150 (2018) 24–28. https://doi.org/10.1016/j.vacuum.2018.01.028.
- [29] A.R. Shugurov, E.D. Kuzminov, A.M. Kasterov, A.V. Panin, A.I. Dmitriev, Tuning of mechanical properties of Ti1–xAlxN coatings through Ta alloying, Surface and Coatings Technology 382 (2020) 125219. https://doi.org/10.1016/j.surfcoat.2019.125219.
- [30] M. Mikula, M. Truchlý, D.G. Sangiovanni, D. Plašienka, T. Roch, M. Gregor, P. Ďurina, M. Janík, P. Kúš, Experimental and computational studies on toughness enhancement in Ti-Al-Ta-N quaternaries, Journal of Vacuum Science & Technology A 35 (2017) 060602. https://doi.org/10.1116/1.4997431.
- [31] G. Greczynski, I. Petrov, J.E. Greene, L. Hultman, Strategy for tuning the average charge state of metal ions incident at the growing film during HIPIMS deposition, Vacuum 116 (2015) 36–41. https://doi.org/10.1016/j.vacuum.2015.02.027.

- [32] G. Greczynski, L. Hultman, Peak amplitude of target current determines deposition rate loss during high power pulsed magnetron sputtering, Vacuum 124 (2016) 1–4. https://doi.org/10.1016/j.vacuum.2015.11.004.
- [33] R. Ganesan, I. Fernandez-Martinez, B. Akhavan, D.T.A. Matthews, D. Sergachev, M. Stueber, D.R. McKenzie, M.M.M. Bilek, Pulse length selection in bipolar HiPIMS for high deposition rate of smooth, hard amorphous carbon films, Surface and Coatings Technology 454 (2023) 129199. https://doi.org/10.1016/j.surfcoat.2022.129199.
- [34] J.A. Santiago, I. Fernández-Martínez, T. Kozák, J. Capek, A. Wennberg, J.M. Molina-Aldareguia, V. Bellido-González, R. González-Arrabal, M.A. Monclús, The influence of positive pulses on HiPIMS deposition of hard DLC coatings, Surface and Coatings Technology 358 (2019) 43–49. https://doi.org/10.1016/j.surfcoat.2018.11.001.
- [35] S.B. Abusuilik, Pre-, intermediate, and post-treatment of hard coatings to improve their performance for forming and cutting tools, Surface and Coatings Technology 284 (2015) 384–395. https://doi.org/10.1016/j.surfcoat.2015.07.003.